How well can we measure the masses, radii and ages of low-mass stars in EBLM systems?

S. Gill, P. F. L. Maxted, B. Smalley

Atrophysics group, Keele University UK
s.gill@keele.ac.uk

Eclipsing binary, low-mass

The Wide Angle Search for Planets (WASP; Pollacco et al. 2006) is a survey for 0.8-2 R_{Jup} objects transiting solar-like stars. Objects in this radius range can have masses which span three orders of magnitude, from Saturn-like planets to M-dwarfs. Consequently, SuperWASP photometry has identified hundreds of FGK stars with transiting M-dwarf companions as a by-product of its successful exoplanet search. These systems are termed EBLMs (eclipsing binary, low-mass).

We have invested considerable effort to characterise these systems, including hundreds of hours of telescope time to measure their spectroscopic orbits. The main aim of the EBLM project (Triaud et al. 2013a; Gómez Maqueo Chew et al. 2014; Triaud et al. 2017; von Boetticher et al. 2017) is to improve our understanding of low-mass stars using accurate mass and radius measurements for transiting companions to FGK stars. So far, four systems (WASP-30, EBLM J1219-39, EBLM J0113+31 and EBLM J0555-57) have been measured. Of these, one star (WASP-30B) appears to be inflated and a second (EBLM J0113+31) is measured to be ~600 K hotter than expected. This latter result comes from an analysis of the secondary eclipses in this system using infrared photometry. A similar result is also seen for KIC1571511 (Ofir et al. 2012) using high-precision optical photometry from the Kepler space telescope. Gómez Maqueo Chew et al. (2014) considered a variety of reasons for an enhanced surface temperature. Although none are these reasons is completely satisfactory, one possible solution may be tidal dissipation of orbital energy in these eccentric binary systems. Such effects have implications for our understanding of the formation of hot Jupiters (Fabrycky & Tremaine 2007).

It is clear that we do not fully understand stars at the bottom of the main sequence and, by implication, the planets orbiting them. With publicity surrounding low mass stars increasing as a result of recent exoplanet discoveries (e.g. TRAPPIST-1 and Proxima Centauri), more effort needs to be invested into understanding what makes some some low-mass stars anomalous so that we can better understand the myriad of exoplanet systems that will be discovered with future space-based missions such as TESS (Ricker et al. 2014a). In this poster we show the extent of which we can measure masses, radii and ages of EBLM systems and present the latest results from the project.

Limb-darkening law

To determine accurate estimates of radii, ratio of radii and impact parameter we required an accurate prescription for limb-darkening in our light-curve model. The EBLM project V (Gill et al. 2018 in prep) used the Claret 4-parameter law (Claret 2000),

$$\frac{I_\lambda(\mu)}{I_\lambda(0)} = 1 - \sum_{i=1}^{4} a_i(1-\mu^{\frac{1}{2}i}),$$

where a_i is the i^{th} limb-darkening coefficient and $\mu = \cos\gamma$, γ being the angle between a line normal to the stellar surface and the line of sight to the observer. An alternative is to use the quadratic limb-darkening law (Kopal 1950) with only 2 parameters,

$$\frac{I_u}{I_0} = 1 - \sum_{i=1}^{2} a_i(1-\mu)^i,$$

and allow both coefficients to vary in a fit using the decorrelated parameters $a_+ = a_1 + a_2$ and $a_- = a_1 - a_2$ (Brown et al. 2001). EBLM V found the majority of stars see a reduction in R_1 below 1% when using the quadratic law instead of the Claret law. The power-2 law has been shown to out-perform other two-coefficient limb-darkening laws (Morello et al. 2017),

$$\frac{I_\mu}{I_0} = 1 - a_1(1-\mu^{-a_2})$$

The EBLM projevt VI (Gill et al. 2018 in prep) used the power-2 limb-darkening law to measure 4 EBLMs observed with Kepler/K2. We interpolate coefficients using tabulated values from the Stagger-grid (Maxted 2018 in prep). One EBLM system is hotter than the Stagger-grid extends (7200 K) and required a synthetic intensity profile to be synthesised using LDTK (Parviainen & Aigrain 2015). The power-2 law was fitted to the intensity profile which was used as priors to fit the light-curve using the decorrelated parameters $h_1 = 1\text{-}a_1(1\text{-}2^{-a2})$ and $h_2 = a_1 2^{-a2}$ (Maxted 2018 in prep).

Contamination

The analysis of 118 EBLM systems in EBLM IV (Triaud et al. 2017) found that 17.8 % of these systems show evidence from drifts in their mean radial velocities of a third body in the system. Lucky imaging provides constraints on nearby contaminating objects. For EBLM J2349–32 and J2308–46, we find that the close companions do not significantly contaminate follow-up photometry. For J0218–31 and J1847+39 we can put constraints on the amount of third light from the consistency between the ratio of the radii measured from transit photometry in different pass-bands. For EBLM J1436–13 we have to rely on existing surveys to identify any nearby stars which may contaminate follow-up photometry. Inspection of the GAIA survey DR1 (resolution of ≤ 1″) finds no evidence of blends or contamination.
Lucky imaging (Fig. 1) typically has a resolution of 0.3″ corresponding to an orbital separation of ≈ 330 AU at the distance of ~200 pc. The three-body systems identified by Triaud et al. (2017) will have orbital period for the outer orbits of decades, corresponding to semi-major axes less than 330 AU. These systems would be difficult or impossible to resolve through lucky imaging. The low signal-to-noise spectra from CORALIE eliminates unresolved blends above 30% contamination by inspection of cross-correlation functions, but we do not have capabilities to identify unresolved companions contributing 10-20 % of the total optical flux.

Including third light as a free parameter in the orbital fit will change the shape and depth of a light-curve; this can lead to degeneracies between R_1/a, k and b. We assessed this by re-fitting the orbital solution for all stars assuming a worst case scenario of 10% light contamination. From this fit, we combine best fitting values of R_1/a, b, and k and their uncertainties with nominal values from the original fit to re-determine R_1 and R_2 from eblmmass. On average, we find a 3-5% increase in R_2 when third light is fixed to 10 %. This is comparable to the inflation in radius for low-mass stars typically quoted in the literature (e.g. 3 – 5%; Spada et al. 2013). However, if we were to see radius inflation in general for the M-dwarf components of EBLM systems then the third-light effect can only be a partial explanation. This is because the majority of these systems do not have third bodies in the system, and the third body will often contribute much less than 10% of the total flux in these triple-star systems.

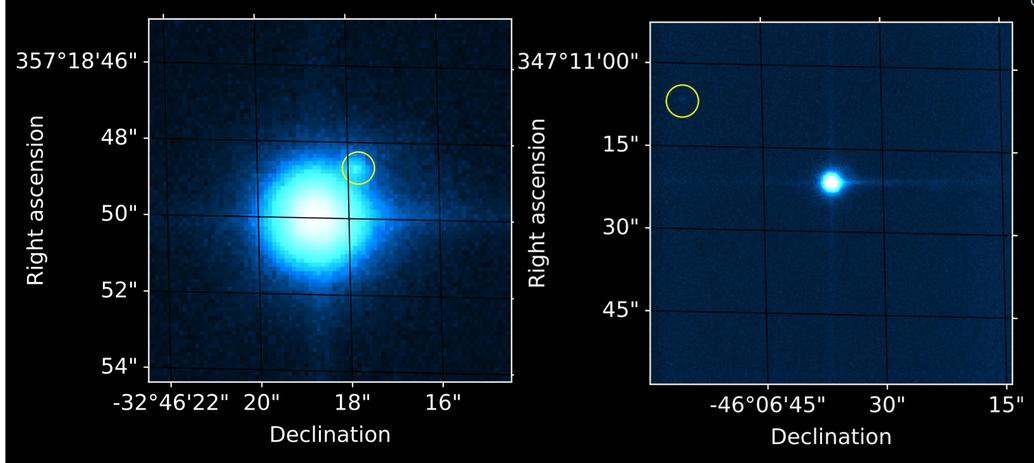

Fig. 1 Lucky imaging of EBLM J2349-32 (left) and J2308-46 (right) from the using the Two Colour Instrument (TCI) on the Danish 1.54-m Telescope at La Silla Observatory.

Star shapes

The ellc lightcurve model uses triaxiial ellipsoids to represent spherical stars. A caveat of this method is that the spherical volume of the star will not be the same as the volume of the triaxial ellipsoid used to approximate its shape (Leconte et al. 2011). We assessed the magnitude of this problem by comparing the models for EBLM J2308-46 where the M-dwarf is described by a sphere to using the Roche models (Fig. 2). We find a maximum difference of ~0.1 ppm owed to the increased mass ratio cf. planets makes the M-dwarf very near spherical. This is far below the white-noise level of ground-based observations (a few thousand ppm) and Kepler/K2 observations (a few hundred ppm) and so a correction for EBLM systems are not required.

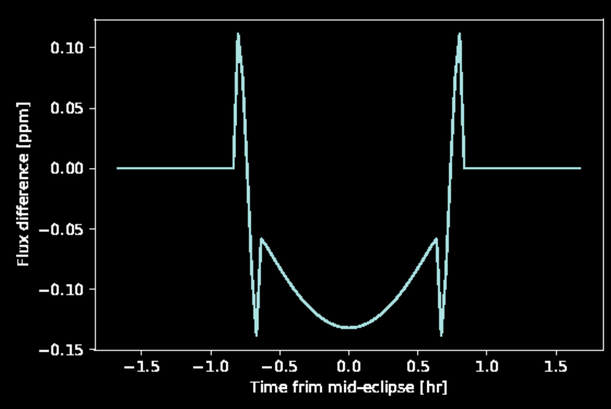

Fig. 2 The difference between the spherical model and Roche model of J2308–46 using ELLC.

Evolution ambiguity

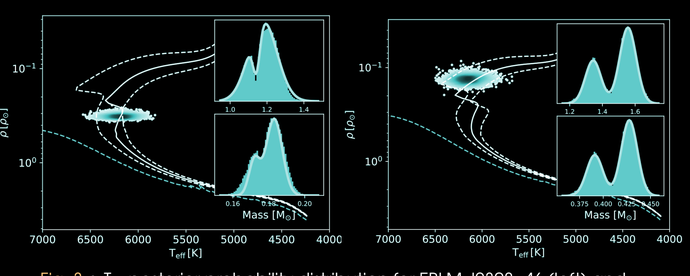

Fig. 3 ρ-T_{eff} posterior probability distribution for EBLM J2308–46 (left) and J0218-31 (right). The zero-age main sequence line (ZAMS) shows the the ρ/T_{eff} values for best fitting model at the start of the stars main sequence lifetime. The isochrone for the best fitting age and $(Fe/H)_i$ is shown with the isochrones for the best fitting $(Fe/H)_i$ and age, plus and minus the uncertainty of age. We also plot the posterior probability distributions for M_1 and M_2 with double-Gaussian fits to estimate M_2 for each model.

The default model grid used in eblmmass uses a mixing length parameter $\alpha_{MLT} = 1.78$ and an initial helium abundance Y = 0.26646 + 0.984 Z, both of which have been calibrated on the Sun. As noted by Maxted et al. (2015a), these assumptions are subject to some level of uncertainty. Maxted et al. (2015b) estimated the uncertainty in mass, M_1, and age, τ, for 28 transiting exoplanet host stars by assuming an error of 0.2 in α_{MLT} and 0.02 for initial helium enhancement, ΔY for each star. They find that systematic errors in mass and age from Y and α_{MLT} can be comparable to the random errors in these values for typical observational uncertainties in the input parameters. We note that the sample used in Maxted et al. (2015b) consists primarily of stars less massive than the Sun, whereas the primary stars in this work are more massive F-type stars. Three grids of models are provided with eblmmass. $\alpha_{MLT} = 1.78$, $\Delta Y = 0.00$ –2. $\alpha_{MLT} = 1.5$, $\Delta Y = 0.00$ – and 3. $\alpha_{MLT} = 1.78$, $\Delta Y = 0.02$. We re-measured the mass, radius and age of both components with the grids 2 and 3 to see how the uncertainties in α_{MLT} and ΔY impact our results. We used grid 2 to asses the impact of $\Delta\alpha_{MLT} = 0.28$ and grid 3 to assess the impact of $\Delta Y = 0.02$.

The mass uncertainties (ΔM_1 and ΔM_2) corresponding to $\Delta\alpha_{MLT} = 0.28$ are ≈ 2 – 3%, and are similar to those found by Maxted et al. (2015b). Helium enhancement typically introduces a larger mass uncertainties ≈ 4 – 5%. The opposite is seen for τ determinations, where a value of $\Delta\alpha_{MLT} = 0.28$ introduces an uncertainty of 1.07 Gyr and $\Delta Y = 0.02$ introduces an uncertainty of $\Delta\tau = 0.86$ Gyr. The typical uncertainty in τ from eblmmass for these EBLM systems is around 1 Gyr which can produce significant systematic offsets. The quadratic combination of uncertainty for M_2 introduced by α_{MLT} and Y is around 0.01 $M_\odot$ (2 – 4 % for a 0.4 $M_\odot$ M-dwarf).

A further limitation arises when the primary star has evolved into post-main sequence blue hook (Henyey hook). Two host-stars in our sample (J2308–46 and J0218–31; Fig. 3) are in this region leading to two distinct solutions for M_1 and τ. A single solution is preferred for both these systems but there will always be some ambiguity until further mass constraints can be obtained. Until then, these systems should not contribute to empirical calibrations. One approach for the EBLM project could be to pre-select cooler host stars ($\lesssim$ 6100 K) to avoid host stars near the Henyey hook. A solution may lie in the increased contrast between a FGK star and an M-dwarf in the infrared. It may be possible to detect molecular lines (VO, TiO, CaH, etc.) associated with an M-dwarf from using high-resolution infrared spectroscopy. This would enable radial velocity measurements of the secondary component, and turn the SB1 into an SB2. This would place a further constraint on which mass and age solution best describes the system.

Current results

<u>EBLM V</u>

For EBLM J2349–32 we have good estimates of the mass and radius for both components and find it is inflated by ≈ 3 % compared to stellar models. For EBLM J1847+39 we only have INT spectra covering the Hα region, leading to a larger uncertainties in (Fe/H), mass and τ of the components in this system compared to the other 4 systems for which we have echelle spectroscopy. For EBLM J0218–31 and J2308–46 we find that the host star has evolved into the post main-sequence blue hook resulting in two solutions for M_1, M_2, & τ (Fig. 3). For each of these systems there is a favoured solution but ambiguity will remain until further constraints on the primary star mass and radius can be obtained. The final system, EBLM J1436–13, shows a grazing transit so the radius estimates for the stars in this system are quite large.

<u>EBLM VI</u>

EBLM J0055-00 has a high impact parameter creating additional uncertainty to the radii of both components in the system (Fig. 5). EBLM J0457+14 is hot (~7200 K) and has a Vsini ~ 70 kms^{-1} resulting in uncertain radial velocity measurements and, by extension, the mass function. The radius of the M-dwarf is inflated by ~ 1-σ compared to models. A secondary eclipse of ~1 mmag corresponded to $T_{eff,2}$ = 3330 K and is consistent with models. J1652-19 has three close companions (~ 14″ east) which are visible in the target pixel files. The brightest of these is around 2.3 mag. fainter and would contribute 5% of the flux if included in the aperture. Full-frame photometry yields a transit depth ~ 0.04 mag. With the companions excluded we measure a transit depth ~ 0.03 mag, corresponding to a change in R_2 from 0.356 $R_\odot$ to 0.317 $R_\odot$. J1652-19 has the best-measured masses and radii of the EBLM VI with uncertainties matching those from EBLM V. This M-dwarf companion is inflated by ~40% (5-σ) compared to evolutionary models and an age of 6 Gyr; far beyond contraction timescales. J2217-04 is the second system in the EBLM VI sample to have measurable secondary eclipses. We calculated a surface temperature of the M-dwarf $T_{eff,2}$ = 3490 K which is consistent with predictions from models. The M-dwarf appears to have a radius consistent with models to 1-σ.

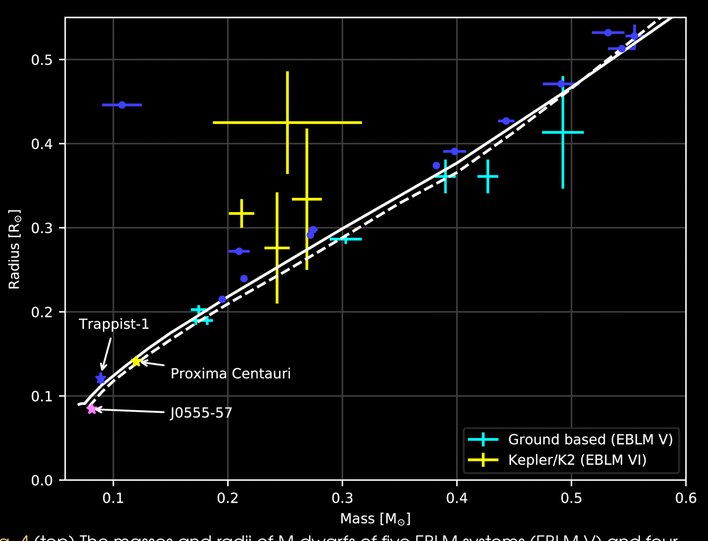

Fig. 4 (top) The masses and radii of M-dwarfs of five EBLM systems (EBLM V) and four Kepler/K2 EBLM systems (EBLM VI). The 5 Gyr isochrone from Baraffe et al. (2015) is plotted (white-line) and the 5 Gyr isochrone for (M/H) = –0.5 (Baraffe et al. 1998) (white-dashed). We plot low-mass stars in well-studied detached eclipsing binaries (black-dot) from DEBCat (Southworth 2015, accessed 8 th Feb 2018). For J2308–46 and J0218–31 we plot both solutions. We also plot Trappist-1 (Delrez et al. 2018), Proxima Centauri (Anglada-Escudé et al. 2016) and J0555–57 (von Boetticher et al. 2017).

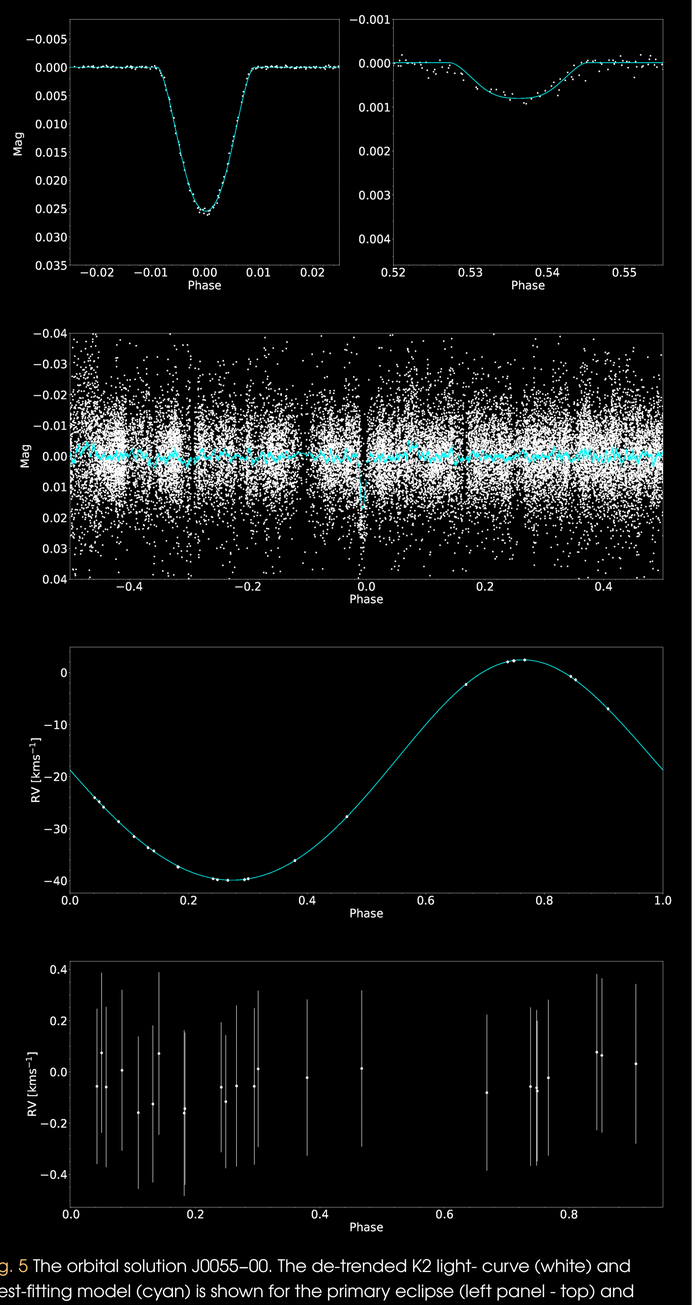

Fig. 5 The orbital solution J0055–00. The de-trended K2 light- curve (white) and best-fitting model (cyan) is shown for the primary eclipse (left panel - top) and secondary eclipse (right panel - top). (upper middle) The SuperWASP photometry (white) and the binned light-curve (100 bins; cyan). (lower middle) Radial velocity measurements (black) with the best-fitting model (red). (bottom) The residuals (observed - calculated) from the radial velocity measurements and the best-fitting model.

EBLMMASS

To estimate the mass and age of the primary star we combined the atmospheric parameters and the best fitting orbital solution and interpolate between evolutionary models computed with the garstec stellar evolution code (Weiss & Schlattl 2008). We use a modified version of the open-source code bagemass (Maxted et al. 2015a) tailored exclusively for EBLM systems (eblmmass). eblmmass uses the jump parameters of age, primary mass (M_1), the initial iron abundance (Fe/H)i , M_2 and the full-width half maximum of the transit w. The vector of observed parameters is given by d = (f(m), T_{eff}, log L_1, $(Fe/H)_s$,R_1/a, w) where log L_1 is the luminosity of the primary star and $(Fe/H)_s$ is the surface metal abundance. The models parameters are d = (M_1, M_2, τ, $(Fe/H)_i$, w). $(Fe/H)_s$ differs from the initial abundance ($(Fe/H)_i$) due to diffusion and mixing processes throughout stellar evolution. The garstec evolutionary models used here are the same as the ones used in bagemass. garstec uses the FreeEOS4 equation of state (Cassisi et al. 2003) and standard mixing length theory for convection (Kippenhahn & Weigert 1990). The mixing length parameter used to calculate the default model grid is $\alpha_{MLT} = 1.78$. With this value of α_{MLT} garstec reproduces the observed properties of the present day Sun assuming that the composition is that given by Grevesse & Sauval (1998), the overall initial solar metallicity is Z = 0.01826, and the initial solar helium abundance is Y = 0.26646. These are slightly different to the value in Serenelli et al. (2013) because we have included additional mixing below the convective zone in order reduce the effect of gravitational settling and so to better match the properties of metal-poor stars. Due to the effects of microscopic diffusion, the initial solar composition corresponds to an initial iron abundance $(Fe/H)_i$ =+0.06. Source code available upon request.

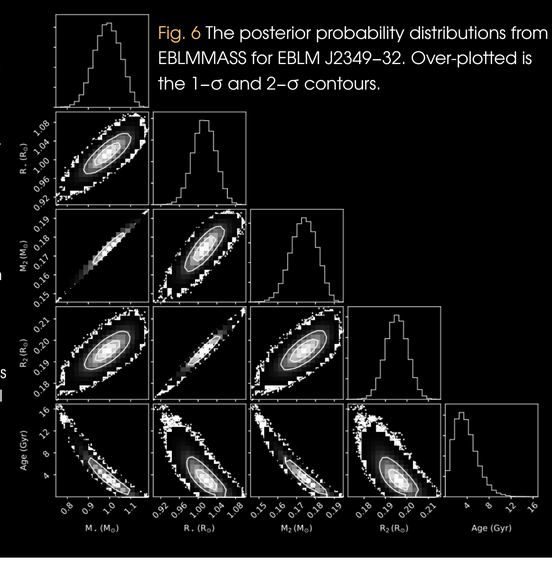

Fig. 6 The posterior probability distributions from EBLMMASS for EBLM J2349–32. Over-plotted is the 1–σ and 2–σ contours.